Tracking the iron K α line and the ultra fast outflow in NGC 2992 at different accretion states

A. Marinucci,[1]⋆ S. Bianchi,[1] V. Braito,[2,3] G. Matt,[1] E. Nardini[4] and J. Reeves[2,5]

[1]*Dipartimento di Matematica e Fisica, Università degli Studi Roma Tre, via della Vasca Navale 84, I-00146 Roma, Italy*
[2]*Center for Space Science and Technology, University of Maryland Baltimore County, 1000 Hilltop Circle, Baltimore, MD 21250, USA*
[3]*INAF – Osservatorio Astronomico di Brera, Via Bianchi 46, I-23807 Merate (LC), Italy*
[4]*Istituto Nazionale di Astrofisica (INAF) – Osservatorio Astrofisico di Arcetri, Largo Enrico Fermi 5, I-50125 Firenze, Italy*
[5]*Astrophysics Group, School of Physical and Geographical Sciences, Keele University, Keele, Staffordshire ST5 5BG, UK*

ABSTRACT

The Seyfert 2 galaxy NGC 2992 has been monitored eight times by *XMM–Newton* in 2010 and then observed again in 2013, while in 2015 it was simultaneously targeted by *Swift* and *NuSTAR*. *XMM–Newton* always caught the source in a faint state (2–10 keV fluxes ranging from 0.3 to 1.6×10^{-11} erg cm^{-2} s^{-1}), but *NuSTAR* showed an increase in the 2–10 keV flux up to 6×10^{-11} erg cm^{-2} s^{-1}. We find possible evidence of an Ultra Fast Outflow with velocity $v_1 = 0.21 \pm 0.01c$ (detected at about 99 per cent confidence level) in such a flux state. The UFO in NGC 2992 is consistent with being ejected at a few tens of gravitational radii only at accretion rates greater than 2 per cent of the Eddington luminosity. The analysis of the low-flux 2010/2013 XMM data allowed us to determine that the Iron K α emission line complex in this object is likely the sum of three distinct components: a constant, narrow one due to reflection from cold, distant material (likely the molecular torus); a narrow, but variable one which is more intense in brighter observations and a broad relativistic one emitted in the innermost regions of the accretion disc, which has been detected only in the 2003 XMM observation.

Key words: accretion, accretion discs – galaxies: Seyfert – galaxies: active – galaxies: individual: NGC 2992.

1 INTRODUCTION

Variability is one of the best tools to investigate the emission mechanisms in active galactic nuclei (AGNs). While in many cases flux variations can be attributed to opacity changes in the line-of-sight absorbers (e.g. NGC 1365 and NGC 1068: Risaliti et al. 2005; Marinucci et al. 2016), a few sources have been observed to vary dramatically in the X-ray intrinsic flux. Highly variable AGNs are the perfect astrophysical laboratories for studying the accretion/ejection mechanisms occurring at different radii in the accretion disc, in response to the primary continuum variations (i.e. at different accretion rates). The profile of the iron K α emission line gives information about the relativistic effects occurring in the innermost regions, about the emissivity of the disc and its ionization state (Fabian et al. 1989; Martocchia & Matt 1996; Fabian et al. 2000; Reynolds & Nowak 2003; Wilkins & Fabian 2012; Reynolds 2014). On the other hand, accretion disc winds ejected at larger radii are investigated by studying the blueshifted absorption features above ∼7 keV (Tombesi et al. 2010, 2011, 2012) and they give us indications on the energetic feedback to the host galaxy (King &

Pounds 2015). Long monitorings in the X-rays (using in particular the XMM spectral resolution combined with the *NuSTAR* broad energy coverage) have provided a number of results in the framework of black hole spin measurements (MCG-6-30-15: Marinucci et al. 2014a; NGC 1365: Walton et al. 2014; SWIFT J2127.4: Marinucci et al. 2014b, Mrk 335: Parker et al. 2014a) and Ultra Fast Outflows measurements (PDS 456: Nardini et al. 2015; IRAS 13224-3809: Parker et al.).

NGC 2992 is a highly inclined ($i = 70°$) spiral galaxy at $z = 0.00771$ (Keel 1996), classified as a Seyfert 1.9/1.5 (Trippe et al. 2008). In the X-rays, it is absorbed by a column density $N_H \sim 9 \times 10^{21}$ cm^{-2} (Hernandez-Garcia et al. 2017, Parker et al. 2014b) and it steadily declined in observed flux from 1978, when it was observed by HEAO1 (Mushotzky 1982) at a flux level of about 8×10^{-11} erg cm^{-2} s^{-1} until 1994, when it was observed by *ASCA* (Weaver et al. 1996) at a flux level by about a factor of 20 fainter (see Fig.1). Then it underwent a rapid recovery: in 1997 it was observed by BeppoSAX at a flux level somewhat higher than in 1994, while in 1998 the source fully recovered its HEAO-1 brightness (Gilli et al. 2000). In 2003, when observed by *XMM–Newton*, the flux was even higher, about 10^{-10} erg cm^{-2} s^{-1}, but the observation was in full-frame mode, and so inevitably piled-up. Nevertheless, an intense
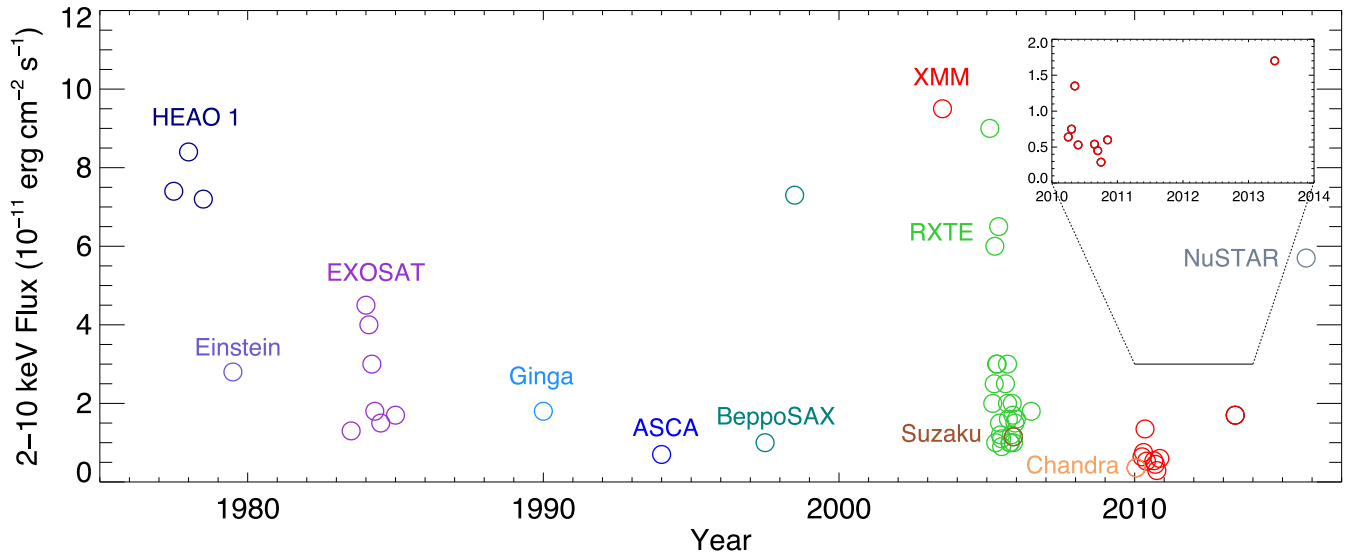
⋆ E-mail: marinucci@fis.uniroma3.it

Figure 1. Historical 2–10 keV light curve of the source. This plot is an extension of the one previously presented in Murphy, Yaqoob & Terashima (2007). The 2010/2013 XMM fluxes are shown in red in the top-right inset.

relativistic component of the iron K α emission line was claimed (Equivalent Width (EW) = 250 ± 70 eV: Shu et al. 2010). The source was then observed by *Suzaku* on 2005 November/December and found in a much fainter state, almost an order of magnitude fainter than in the *XMM–Newton* observation. Both an unresolved and a broad component of the iron line were detected (Yaqoob et al. 2007). The time behaviour of the iron line is very interesting, suggesting the presence of a relativistic component that becomes more extreme at high flux levels. Notably, this behaviour is the opposite of what is observed in other sources with relativistic lines and explained in the framework of the light bending model (Martocchia & Matt 1996; Miniutti & Fabian 2004).

The *RXTE* monitoring campaign (Fig. 1) consisted of 24 pointings between early March 2005 and late January 2006, with the interval between observations ranging from 3 to 33 d. Large amplitude (almost an order of magnitude) variability was found, indicating that the variability time-scale is quite short, of the order of days, while no significant variation of the primary power-law index was found. Similar flux variations, up to a factor of ∼10, are also apparent in the *Swift*/BAT light curve. Two flares (with 2–10 keV fluxes $F_{\rm x}$ = 3.6×10^{-10} erg cm^{-2} s^{-1}) have been recently measured on 2016 June 2 and on 2014 April 14 by the MAXI team in a sky position consistent with NGC 2992 (Negoro et al. 2016). In 2010, NGC 2992 was observed eight times for ∼40 ks by *XMM–Newton* and three times by *Chandra* (Murphy, Nowak & Marshall 2017), with a 2–10 keV flux ranging from 3×10^{-12} erg cm^{-2} s^{-1} (its historical minimum) to 1.3×10^{-11} erg cm^{-2} s^{-1}. A further 2013 *XMM–Newton* observation caught the source in a similarly low-flux state (1.6×10^{-11} erg cm^{-2} s^{-1}). The most recent X-ray observation of this object was performed simultaneously with *Swift* and *NuSTAR* in 2015 and a 2–10 keV flux of ∼6×10^{-11} erg cm^{-2} s^{-1} was measured. As suggested by Yaqoob, Murphy & Terashima (2007), the overall behaviour suggests a scenario in which the accretion disc becomes more radiatively efficient at high luminosities, making NGC 2992 one of the few sources in which the broad, relativistic component of the iron K α is seen to respond to nuclear variations.

We hereby analyse the latest XMM, *Swift,* and *NuSTAR* spectra, with the aim of understanding the physical scenario beneath this puzzling source. The paper is structured as follows. In Section

Table 1. Observation log for the NGC 2992 observations with *XMM–Newton* (2010–2013), *NuSTAR*, and *Swift* (2015). XMM and *Swift* count rates are inferred in the 0.5–10 keV energy band, while for *NuSTAR* we used 3–79 keV.

Obs. ID	Date	Time (ks)	Count rate (cts s^{-1})	Region (arcsec)
0654910301	2010-05-06	41.1	1.304 ± 0.170	25
0654910401	2010-05-16	40.2	1.526 ± 0.049	39
0654910501	2010-05-26	38.5	2.688 ± 0.018	35
0654910601	2010-06-05	38.7	1.094 ± 0.096	28
0654910701	2010-11-08	38.8	1.146 ± 0.041	40
0654910801	2010-11-18	35.8	0.953 ± 0.037	36
0654910901	2010-11-28	37.5	0.641 ± 0.076	26
0654911001	2010-12-08	42.0	1.218 ± 0.061	37
0701780101	2013-05-11	9.0	3.301 ± 0.047	40
60160371002	2015-12-02	20.8	2.411 ± 0.047	50
00081055001	2015-12-02	6.5	0.809 ± 0.010	120

2, we discuss the observations and data reduction. In Section 3, we present the spectral analyses. We discuss and summarize the physical implications of our results in Sections 4 and 5.

2 OBSERVATIONS AND DATA REDUCTION

2.1 *XMM–Newton*

NGC 2992 ($z = 0.0071$) has been subject to a monitoring campaign with *XMM–Newton* (Jansen et al. 2001) in 2010, starting on 2010 May 6 with the EPIC CCD cameras, the Pn (Strüder et al. 2001) and the two MOS (Turner et al. 2001), operated in small window and thin filter mode. Data from the MOS detectors are not included in our analysis due to the lower statistics of the spectra. The extraction radii and the optimal time cuts for flaring particle background were computed with SAS 16 (Gabriel et al. 2004) via an iterative process which leads to a maximization of the SNR, similar to the approach described in Piconcelli et al. (2004). The resulting optimal extraction radii, net exposure times, count rates and ObsIDs are listed in Table 1, and the background spectra were extracted from

source-free circular regions with a radius of 50 arcsec. The 2003 observation (ObsID 0147920301) is heavily affected by pile-up, and we therefore considered a source extraction annulus from 10 to 40 arcsec to remove this effect. After careful inspection of the *epatplot* output, confirming the goodness of the data, the net exposure time is 23 ks. This is in agreement with the previous analysis of this data set presented in Shu et al. (2010).

Spectra were then binned in order to oversample the instrumental resolution by at least a factor of 3 and to have no less than 30 counts in each background-subtracted spectral channel. Light curves in the 0.5–2 keV, 0.5–10 keV bands and hardness ratios can be seen in Fig. 2: since no significant spectral variability is observed within each observation we used time averaged spectra. We adopt the cosmological parameters $H_0 = 70 \, \mathrm{km \, s^{-1} \, Mpc^{-1}}$, $\Omega_\Lambda = 0.73$, and $\Omega_m = 0.27$, i.e. the default ones in XSPEC 12.9.0 (Arnaud 1996). Errors correspond to the 90 per cent confidence level for one interesting parameter ($\Delta \chi^2 = 2.7$), if not stated otherwise.

2.2 *NuSTAR*

NuSTAR (Harrison et al. 2013) observed NGC 2992 with its two coaligned X-ray telescopes with corresponding Focal Plane Module A (FPMA) and B (FPMB) on 2015 December 2 for a total of ~37.4 ks of elapsed time, respectively. The Level 1 data products were processed with the *NuSTAR* Data Analysis Software (NuSTAR-DAS) package (v. 1.7.1). Cleaned event files (level 2 data products) were produced and calibrated using standard filtering criteria with the NUPIPELINE task and the latest calibration files available in the *NuSTAR* calibration database (CALDB 20170720). Extraction radii for the source and background spectra were 50 and 70 arcsec, respectively. After this process, the net exposure times for the two observations were 20.8 ks. Count rates, ObsID, and net exposure time are summarized in 1. The two *NuSTAR* spectra were binned in order to oversample the instrumental resolution by at least a factor of 2.5 and to have a signal-to-noise ratio (SNR) greater than 5σ in each spectral channel. A cross-calibration factor $K_1 = 1.017 \pm 0.013$ between the two detectors is found.

2.3 *Swift*

As part of the *Swift*-BAT AGN survey, the source has been also observed by *Swift* XRT on 2015 December 2, simultaneously to *NuSTAR*. Using a 120 arcsec radius circular region centred on the source we find a count rate of 0.81 ± 0.01 cts s^{-1} in the whole energy band, which is greater than the ~0.6 cts s^{-1} threshold for pile-up (Moretti et al. 2004; Vaughan et al. 2006). Following the online guideline[1] we excluded the central 8 arcsec and used a background region of 120 arcsec radius. The resulting spectrum was binned in order to oversample the instrumental resolution by at least a factor of 3 and to have at least 30 counts in each spectral channel. We allowed for a cross-calibration constant $K_2 = 0.97 \pm 0.05$ between XRT and FPMA spectra.

3 SPECTRAL ANALYSIS

3.1 The 2010–2013 *XMM–Newton* low flux states

We start our spectral analysis of the 2010/2013 XMM data by fitting the 5–10 keV spectra with the aim of searching for variations of the

[1] http://www.swift.ac.uk/analysis/xrt/pileup.php

iron K α line. As a first step, we only leave the continuum free to vary and lines parameters tied. We used an absorbed power law and 5 Gaussians to model the following emission lines: neutral Fe K α and K β, Fe XXV He α, Fe XXVI Ly α, and Ni K α. We also included a ZASHIFT component in XSPEC to take into account the mis-calibration of the EPIC-pn CTI (see Marinucci et al. 2014b; Cappi et al. 2016; Nardini et al. 2016, for Ark 120, NGC 5548 and MCG-6-30-15, respectively). At this stage, the only variable parameters are the power-law slope and normalization, the absorbing column density and the shift of the lines. We obtain a good χ^2/d.o.f. = 556/516 = 1.07. To search for variations between the nine observations, we allow fluxes and energy centroids of the emission lines free to adjust: a χ^2/d.o.f. = 516/507 = 1.01 is retrieved. Fluxes and EWs are plotted in Fig. 3. Best-fitting values for emission lines other than the neutral Fe K α will be further discussed at the end of this section. Fig. 3 (left-hand panel) shows that the flux of the narrow Fe K α is constant among the nine observations, with the exception of Obs 3 and 9, and the best-fitting value $(2.2 \pm 0.2 \times 10^{-5}$ ph cm^{-2} s^{-1}) is in perfect agreement with the one found with *Chandra* HETG (Murphy et al. 2017). The change of the iron K α flux in Obs 3 and 9 suggests either a variation of the Compton-thick reflector or the appearance of a new spectral component. Since a further, broad iron K α component, arising from the innermost regions of the accretion disc was found in past *Suzaku* and XMM data (Yaqoob et al. 2007; Shu et al. 2010), we tried to include it in our fits, fixing the narrow iron Kα to the combined best-fitting value. The additional 6.4 keV lines are unresolved: only upper limits for the widths $\sigma_3 < 70$eV and $\sigma_9 < 90$eV for Obs 3 and 9 are found, respectively. The corresponding fluxes are $F_3 = 0.6 \pm 0.3 \times 10^{-5}$ and $F_9 = 1.4 \pm 0.6 \times 10^{-5}$ ph cm^{-2} s^{-1}. These width of the lines are converted into velocities $v_3 < 7700$ km s^{-1} and $v_9 < 9900$ km s^{-1} (FWHM), suggesting that the additional component could be due to material located in the Broad Line Region but not in the inner accretion disc. For completeness, we also included in the plots the best-fitting parameter of the same model applied to 2014 *NuSTAR* data.

We then extended the analysis down to 0.5 keV modifying the model as follows. We included an absorbed primary component (ZWABS∗CUTOFFPL in XSPEC) and cold reflection from distant material (XILLVER: García et al. 2013). We linked the photon index and high-energy cut-off of XILLVER to the ones of the CUTOFFPL component, fixing the inclination angle to 30 deg, only the reflected spectrum is taken into account. Throughout the paper, we will use the reflection fraction (i.e. the fraction of the illuminating continuum which is Compton scattered) as the ratio between the 10 and 50keV luminosities: $R = L_{\mathrm{refl}}/L_{\mathrm{int}}$. Due to the limited XMM energy band, the high-energy cut-off is fixed to 500 keV. A soft X-ray scattered component below ~2 keV from gas photoionized by the nuclear continuum, possibly associated with the Narrow Line Region (NLR) (Bianchi, Guainazzi & Chiaberge 2006; Guainazzi & Bianchi 2007) has been included. We produced a grid model for XSPEC using CLOUDY 17 (last described by Ferland et al. 2017). It is an extension of the same model used in Bianchi et al. (2010) and Marinucci et al. (2011, 2017). Grid parameters are log U = [− 2.00: 4.00], step 0.25, log N_{H} = [19.0: 23.5], step 0.1. Only the reflected spectrum, arising from the illuminated face of the cloud, has been taken into account in our model. The whole model has been then multiplied by a Galactic absorption of 4.8×10^{20} cm^{-2} (Kalberla et al. 2005). We also included an APEC model to reproduce the thermal emission from extra-nuclear material previously observed with *Chandra* at low energies (Colbert et al. 2005). At this stage of the spectral analysis, the photon index is initially fixed to
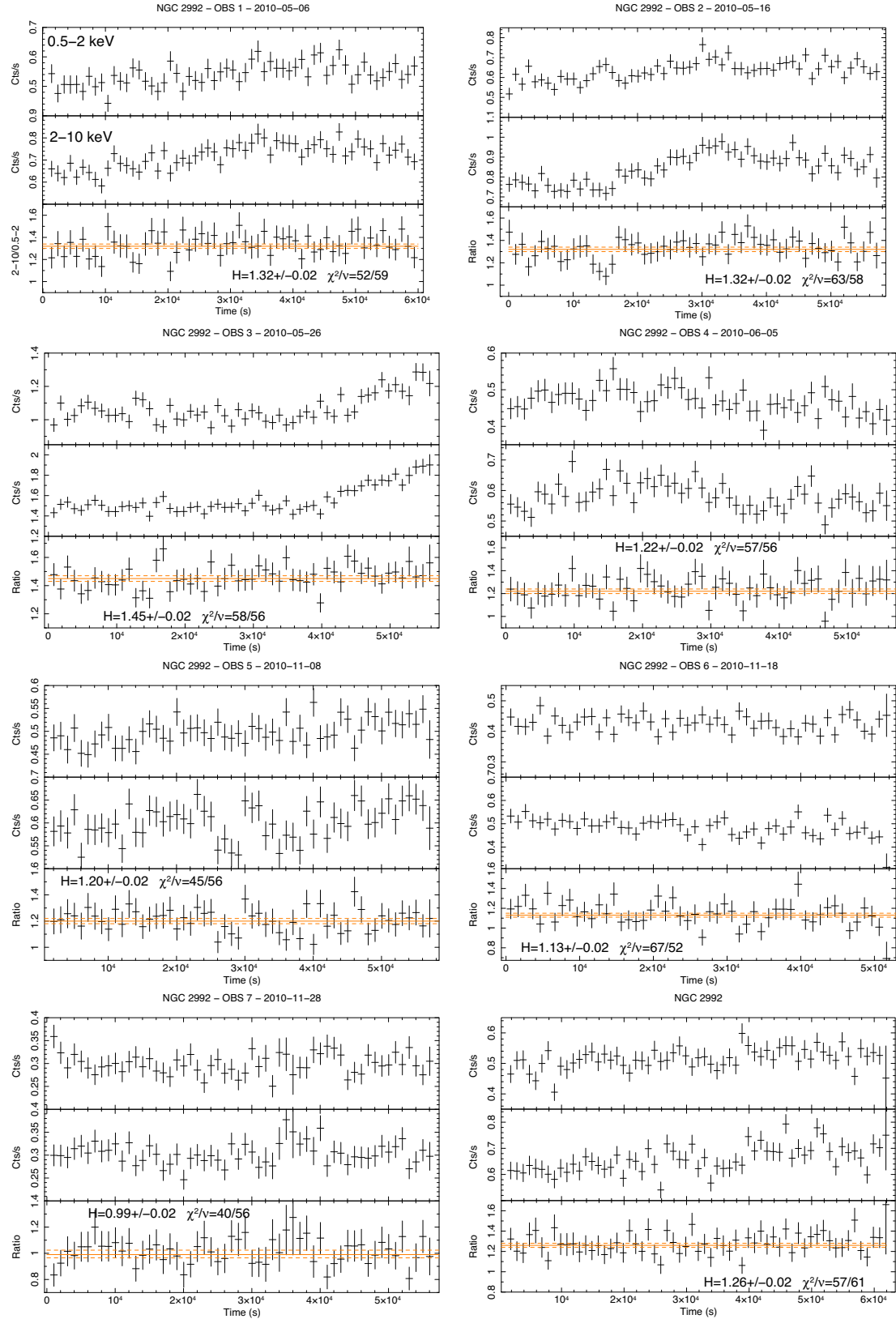
Figure 2. Light curves and hardness ratios for the eight observations of the XMM monitoring campaign. We used a time binning of 1000 s.

$\Gamma = 1.7$, the normalization of the Compton reflection (XILLVER) is tied between the nine observations and the fluxes of the emission lines in the 6.5–7.5 keV interval are free. Due to the variable intrinsic flux of the source, we also left the absorbing column density
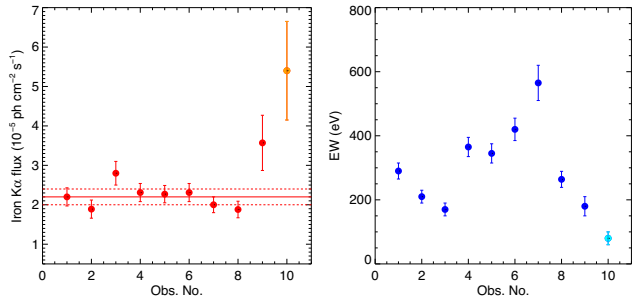
Figure 3. Temporal behaviour of the Fe K α flux and EW (when only a single, narrow component of the line is included in the model). Horizontal solid and dashed red lines indicate best-fitting value and error bars when the Fe K α flux is tied between the nine spectra. Red and blue data points are XMM pointings; orange and cyan refer to *Swift-NuSTAR* data. We adopted 1σ error bars.

and power-law normalization free to vary. The extra-nuclear, soft emission parameters ($\log U$, $\log N_{\rm H}$, normalization in CLOUDY and kT, normalization in APEC) are tied between the nine observations. The reduced χ^2 is decent (χ^2/d.o.f. = 1727/1351 = 1.28), but some residuals can be found around $\sim$1 keV and above 5 keV. The inclusion of a narrow Gaussian improves the fit ($\Delta\chi^2 = -76$ for two additional degrees of freedom) with a resulting energy $E = 1.05 \pm 0.03$ keV and flux $F = 0.5 \pm 0.1 \times 10^{-5}$ ph cm^{-2} s^{-1} and consistent with a blend of Ne X K α and Fe XVII 4C emission lines. Detailed modelling of the soft X-ray emission lines is beyond the purpose of this paper and will be addressed, taking into account the RGS spectra, in a forthcoming paper. We then left the XILLVER normalization and the photon index free to change between the observations, with statistical improvements $\Delta\chi^2 = -175/8$ d.o.f. and $\Delta\chi^2 = -92/9$ d.o.f., respectively. We obtain a best-fitting χ^2/d.o.f. = 1384/1332 = 1.03. Best fits, spectra, and residuals can be seen in Fig. 4 and Table 2. Best-fitting parameters for the soft X-ray emission are $\log U = 1.68^{+0.10}_{-0.14}$, $\log (N_{\rm H}/{\rm cm}^{-2}) = 21.1^{+0.2}_{-0.3}$ and $kT = 0.45 \pm 0.05$, for the CLOUDY and APEC components, respectively. Their 0.5–2.0 keV observed luminosities are $L_{\rm CL} = 1.8^{+1.3}_{-0.7} \times 10^{40}$ erg s^{-1} and $L_{\rm AP} = 6.8^{+1.0}_{-0.6} \times 10^{39}$ erg s^{-1}.

The amount of Compton reflection (i.e. the 2–10 keV flux of the XILLVER component) is plotted against the intrinsic nuclear flux in Fig. 5, and solid and dashed horizontal lines indicate best-fitting value and error bars when all the low flux data are simultaneously fitted (1.25 $\pm$ 0.08 $\times$ 10^{-12} erg cm^{-2} s^{-1}). Deviations from this value are found for two observations only (Obs 3 and 9, see also Table 2), and this might be indicative of a response from the circumnuclear material to the primary continuum variations. While this solution is unlikely for Obs 3 (2010-05-26) due to the short time scales between the previous and following observations (2 weeks), it could be viable for the 2013 observation. We note, however, that some residuals are still found around the iron K α energy, and when an additional component is added ($\Delta\chi^2 = -10$ for one additional degree of freedom), the 2–10 keV XILLVER flux is consistent with being constant. We show, in the right-panel panel of Fig. 5, the 2–10 keV flux of the XILLVER component against the total flux of the iron K α emission line, from the previous analysis. The linear correlation between the two parameters clearly suggests that the XILLVER component is trying to compensate for the variations of a different Fe K component (similar to the Iron line behaviour observed in the recent XMM campaign of Ark 120: Nardini et al. 2016). We conclude that the reflected emission arising from cold, distant material is constant throughout the nine observations.

Best-fitting values for energy centroids of Fe XXV He α, Fe XXVI Ly α, and Ni K α (which are not accounted for by XILLVER) are $E_1 = 6.77 \pm 0.09$, $E_2 = 7.00 \pm 0.05$, and $E_3 = 7.55 \pm 0.08$ keV, respectively. No statistically significant variations are found between the nine observations and their fluxes are always consistent with the ones found in the lowest state spectrum (observation 7): $F_1 = 0.22 \pm 0.09 \times 10^{-5}$, $F_2 = 0.23 \pm 0.11 \times 10^{-5}$, and $F_3 = 0.25 \pm 0.13 \times 10^{-5}$ ph cm^{-2} s^{-1}.

3.2 The 2015 *Swift+NuSTAR* medium flux state

The baseline model used for the 2010 XMM spectra is then applied to the simultaneous 2015 *Swift+NuSTAR* observation. Soft X-ray emission parameters are fixed to the combined XMM fit. The resulting χ^2/d.o.f. is good (418/416), and a Compton reflection fraction $R = 0.18 \pm 0.07$ from cold material is measured, consistent with the flux of the constant XMM reflection component. Residuals around the neutral iron K α line and $\sim$8 keV are present (Fig. 6, top panel).

The inclusion of two Gaussians to reproduce both emission and absorption lines leads to a best-fitting χ^2/d.o.f. = 373/411. The best fit to the data set with corresponding residuals are shown in Fig. 7, while best-fitting parameters are reported in Table 3. The broad iron K α emission line is found at 6.32 $\pm$ 0.12 keV, with a flux $F = 7.0 \pm 2.5 \times 10^{-5}$ ph cm^{-2} s^{-1} and a width $\sigma = 250^{+190}_{-120}$ eV (with a statistical significance greater than 99.99 per cent, accordingly to the *F*-test). We show, in Fig. 8, the residuals when the continuum and the broad iron K α model is applied to the *NuSTAR* data in the 3–10 keV interval. The absorption line is clearly visible in the bottom panel and it is found at $8.26^{+0.09}_{-0.12}$ keV (rest-frame energy), with a flux $F = -1.8 \pm 0.8 \times 10^{-5}$ ph cm^{-2} s^{-1} (with a statistical significance greater than 99.7 per cent). The inclusion of the broad iron K α component is accompanied by a drop in the Compton reflection fraction ($R < 0.08$). This width corresponds to a velocity $v \simeq 28^{+22}_{-14} \times 10^3$ km s^{-1} and is consistent with material orbiting with Keplerian motion located in the outskirts of the accretion disc or in the inner regions of the BLR. The best-fitting power-law index is $\Gamma = 1.72 \pm 0.03$ and only a lower limit for the high-energy cut-off $E_{\rm c} > 350$ keV is found. Another solution could be an iron K α line smeared by relativistic effects, as already discussed for the 2003 XMM high flux state of the source in Shu et al. (2010). We therefore tried to model the broad-line component in terms of relativistic reflection (using the RELXILL model in XSPEC; Dauser et al. 2013). The inclination of the disc is fixed to 30 deg and standard values for the emissivity are assumed ($\epsilon(r) \propto r^{-3}$). The best-fitting solution requires a high value for the iron abundance ($A_{\rm Fe} > 7$) because of the modest Compton reflection associated with the line. The best fit reduced χ^2 is statistically equivalent to the one inferred above χ^2/d.o.f. = 371/411 and the relativistic line has to be produced at a radius $r > 35\, r_{\rm g}$. The upper limit for the cold, distant Compton reflection becomes $R < 0.03$.

In both scenarios, the reflection fraction is very low and the dominant spectral component is the primary power-law continuum (with a $\Gamma = 1.72 \pm 0.03$). We therefore find the same intensity and energy centroid for the UFO feature adopting the two different models.

3.3 The 2003 *XMM–Newton* high-flux state

We first apply a model composed of an absorbed primary continuum and soft X-ray, extra-nuclear emission [TBABS×(ZWABS×CUTOFFPL + APEC + CLOUDY)] to the XMM high-flux state spectrum. We find a
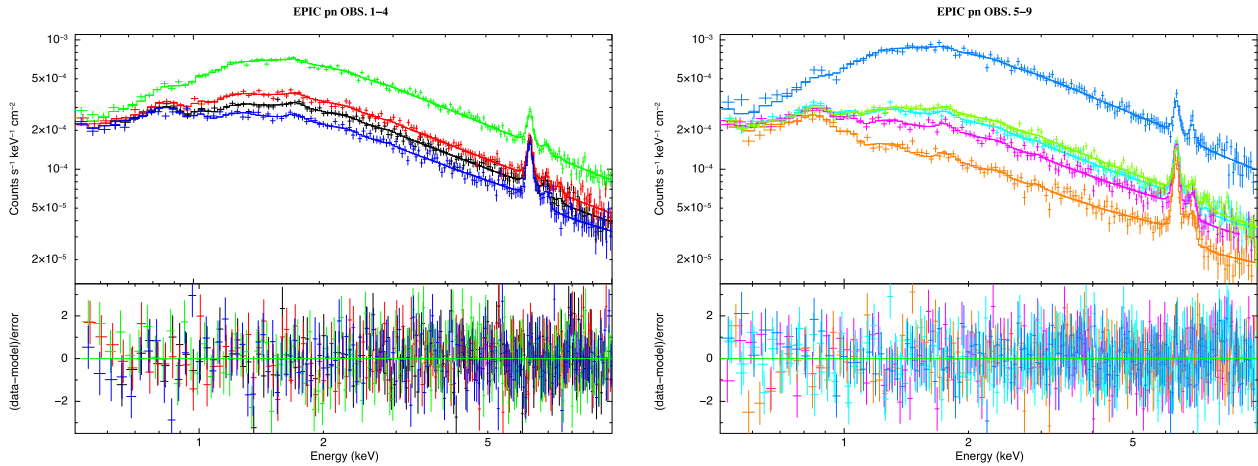
Figure 4. EPIC pn best fits, with associated residuals. All spectra are divided by the effective area of the instrument, for plotting purposes only.

Table 2. Best-fitting parameters of the combined XMM analysis. Luminosities are corrected for absorption.

| Obs date	Best-fitting parameter						
	N_H ($\times 10^{22}$ cm^{-2})	Γ	N_{pow} ($\times 10^{-3}$)	N_{xill} ($\times 10^{-4}$)	R	$F_{2-10\,keV}$ ($\times 10^{-11}$ erg cm^{-2} s^{-1})	$L_{2-10\,keV}$ ($\times 10^{42}$ erg s^{-1})
2010-05-06	0.92 ± 0.06	1.67 ± 0.05	1.30 ± 0.05	1.04 ± 0.08	1.65 ± 0.20	0.65 ± 0.03	0.90 ± 0.05
2010-05-16	0.86 ± 0.05	1.64 ± 0.04	1.50 ± 0.07	1.01 ± 0.08	1.25 ± 0.15	0.75 ± 0.02	1.05 ± 0.05
2010-05-26	0.84 ± 0.04	1.61 ± 0.04	2.78 ± 0.08	1.45 ± 0.15	0.90 ± 0.15	1.35 ± 0.02	1.90 ± 0.10
2010-06-05	0.85 ± 0.08	1.67 ± 0.05	1.00 ± 0.05	1.07 ± 0.07	2.25 ± 0.35	0.53 ± 0.03	0.75 ± 0.05
2010-11-08	0.80 ± 0.07	1.67 ± 0.05	1.03 ± 0.05	1.10 ± 0.07	2.20 ± 0.25	0.54 ± 0.03	0.75 ± 0.04
2010-11-18	0.80 ± 0.08	1.70 ± 0.06	0.80 ± 0.05	1.10 ± 0.07	3.10 ± 0.50	0.45 ± 0.02	0.65 ± 0.05
2010-11-28	0.81 ± 0.10	1.71 ± 0.09	0.45 ± 0.04	0.85 ± 0.10	4.50 ± 1.10	0.30 ± 0.02	0.40 ± 0.03
2010-12-08	0.90 ± 0.06	1.68 ± 0.04	1.20 ± 0.06	0.95 ± 0.07	1.65 ± 0.20	0.60 ± 0.02	0.85 ± 0.03
2013-05-11	0.81 ± 0.05	1.63 ± 0.06	3.45 ± 0.05	1.78 ± 0.28	0.96 ± 0.20	1.65 ± 0.05	2.30 ± 0.10
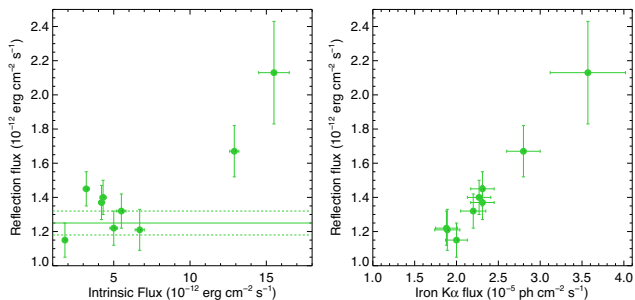
Figure 5. *Left-hand panel:* 2–10 keV fluxes for the reflection and primary components are shown. Solid and dashed lines indicate best-fit value and error bars when data are fitted simultaneously, excluding observation 3 and 9 (i.e. the ones with intrinsic fluxes greater than 1×10^{-11} erg cm^{-2} s^{-1}). *Right-hand panel:* 2–10 keV fluxes for the reflection component is plotted against the flux of the Iron K α emission line.

power law with $\Gamma = 1.76 \pm 0.02$ absorbed by a column density $N_H = 0.7 \pm 0.1 \times 10^{22}$ cm^{-2} and no statistically significant difference for the CLOUDY and APEC parameters, with respect to the ones presented in Section 3.1. We show, in the bottom panel of Fig. 6, contour plots between the normalization and the energy centroid of a Gaussian line left free to vary in the 5–10 keV range. Both emission features (narrow and broad) at ~6.4keV and absorption ones above 8 keV can be clearly seen. The inclusion of a cold reflection component responsible for the narrow iron K α line ($R =$

0.36 ± 0.06) leads to a χ^2/d.o.f. $= 261/162 = 1.6$ with an improvement $\Delta\chi^2 = -139$ for one degree of freedom. We modelled the broad relativistic component in terms of a simple Gaussian line and our best-fitting values ($E_{br} = 6.0^{+0.2}_{-0.4}$ keV, $F_{br} = 2.4^{+0.8}_{-0.4} \times 10^{-4}$ ph cm^{-2} s^{-1}, EW$_{br} = 230^{+60}_{-40}$ eV) are in perfect agreement with Shu et al. (2010), leading to a χ^2/d.o.f. $= 203/159 = 1.3$. Residuals to this fit are shown in the middle panel of Fig. 9, suggesting the presence of multiple absorption lines above 8 keV. We therefore included three narrow, unresolved Gaussians with variable energy and flux: best-fitting values for the rest-frame energy centroids, fluxes, EW, and fit improvements are shown in Table 4. The final goodness of fit χ^2/d.o.f. $= 160/151 = 1.06$ and we find a steeper continuum ($\Gamma = 1.82 \pm 0.02$) with respect to the 2010 *XMM–Newton* spectra. We note, however, that a statistically comparable fit is obtained if a single broad absorption line ($\sigma = 0.30^{+0.22}_{-0.15}$ keV) is adopted at $9.47^{+0.20}_{-0.15}$ keV with an EW $= -180^{+80}_{-120}$ eV. We will discuss the physical interpretation of this component in Section 3.5. None of these absorption lines are present in the nine 2010/2013 XMM low-flux spectra and the inclusion of an absorption line at 8.26 keV only leads to lower limits on its flux ($F_{abs} > -4 \times 10^{-6}$ ph cm^{-2} s^{-1} in Obs 3).

3.4 Statistical significance of absorption lines

It is widely known that in order to assess the statistical significance of narrow unresolved features, standard likelihood ratio tests might lead to inaccurate results (Protassov et al. 2002). We there-
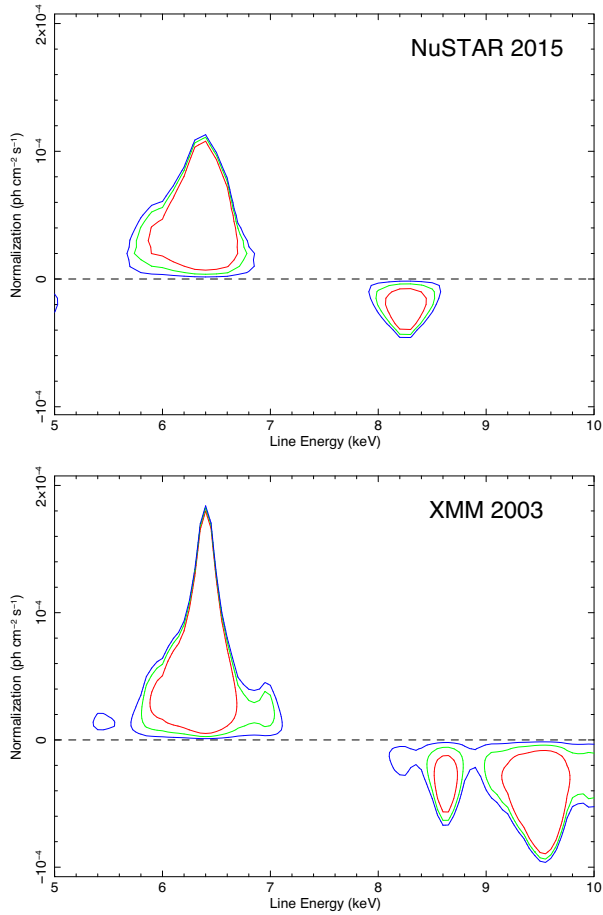
Figure 6. Contour plots at 68 per cent, 90 per cent, and 99 per cent confidence levels ($\Delta\chi^2 = 2.3$, 4.61, and 9.21, respectively) between the normalization and line energy when a Gaussian is left free to vary in the 5–10 keV energy range, for the 2015 *NuSTAR* (FPMA and FPMB, top panel) and 2003 XMM high-flux observations (bottom panel). The adopted model for the continuum is composed of an absorbed power law.
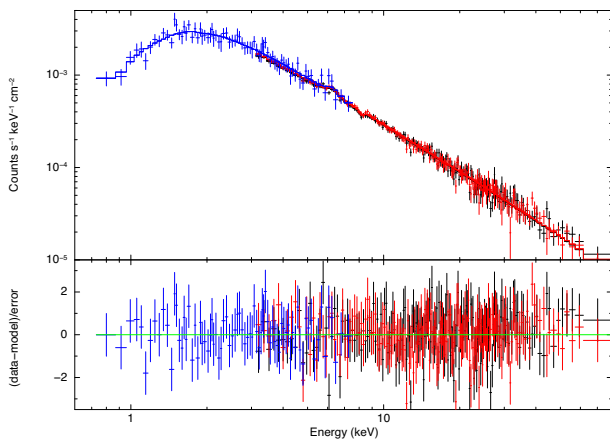

Figure 7. Best fit of the simultaneous *Swift–NuSTAR* data. Residuals are shown in the bottom panel.

Table 3. Best-fitting parameters of the combined *Swift–NuSTAR* analysis.

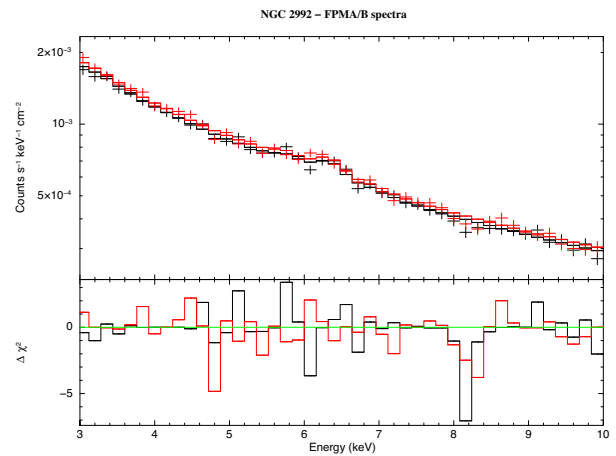| Parameter	Best-fitting value
N_H ($\times 10^{22}$ cm^{-2})	1.1 ± 0.2
Γ	1.72 ± 0.03
E_c (keV)	>350
N_{pow} ($\times 10^{-2}$)	1.62 ± 0.07
N_{xill} ($\times 10^{-5}$)	<5.5
$F_{2-10\,keV}$ (erg cm^{-2} s^{-1})	$5.8 \pm 0.3 \times 10^{-11}$
$L_{2-10\,keV}$ (erg s^{-1})	$7.6 \pm 0.3 \times 10^{42}$

Figure 8. The fit of the continuum model and the broad iron K α applied to the data is shown in the 3–10 keV band. We do not include *Swift* data for the sake of visual clarity. The 8.26 keV absorption line is clearly visible in both FPM detectors.
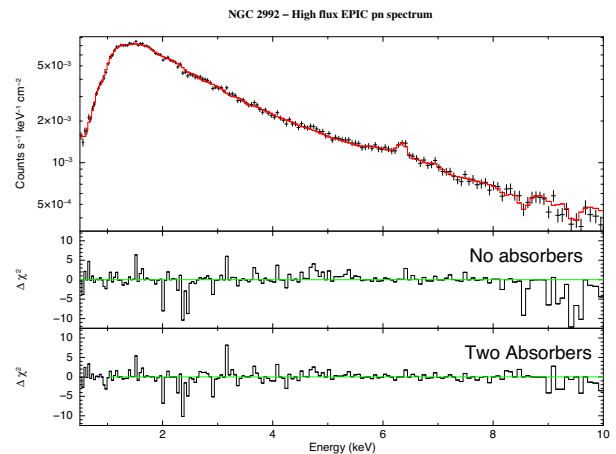

Figure 9. Best fit to the 2003 high-flux EPIC pn data and residuals are shown when a model with no absorbers (middle panel) and with the inclusion of two absorbers (bottom panel) is considered.

fore followed the approach discussed in Tombesi et al. (2010) and Walton et al. (2016) to produce Monte Carlo simulations of our data sets and to retrieve a statistical significance for each absorption line detected. We produced 10 000 fake data sets of the *NuSTAR* FPMA/B or *XMM–Newton* EPIC pn spectra for each of the four absorption lines reported in Table 4, using the FAKEIT command in XSPEC. Responses, background files, exposure times, and energy binning are the same as the ones used for real data. We considered the best-fitting models presented in Sections 3.2 and 3.3 without

Table 4. Best-fitting parameters for the two absorbing layers, energies are reported in the rest-frame of the source. The statistical significance of the four absorption lines is calculated via Monte Carlo simulations (see 3.4 for details).

	Energy (keV)	Flux (10^{-5} ph cm^{-2} s^{-1})	EW (eV)	Significance σ	v_{out}/c	$\Delta\chi^2$/d.o.f.
2015	$8.26^{+0.09}_{-0.12}$	-1.8 ± 0.8	-45 ± 20	2.6	0.21 ± 0.01	$-9/2$
2003	8.61 ± 0.05	-2.2 ± 1.2	-40 ± 25	2.7	0.209 ± 0.006	$-9/2$
	9.27 ± 0.10	-2.0 ± 1.3	-45 ± 30	1.9	0.31 ± 0.01	$-8/2$
	9.57 ± 0.06	-3.3 ± 1.3	-70 ± 25	3.6	0.307 ± 0.006	$-26/2$
	$\log N_H$ (cm^{-2})	$\log U$	v_{out}/c	$\dot{M}_{out}$ (g s^{-1})	$\dot{E}_k$ (erg s^{-1})	$\dot{p}_{out}$ (g cm s^{-2})
2015	22.25 ± 0.25	2.45 ± 0.25	0.21 ± 0.01	3.5×10^{23}	6.9×10^{42}	2.2×10^{33}
2003	$23.35^{+1.10}_{-0.55}$	>3.1	0.215 ± 0.005	3.8×10^{24}	7.9×10^{43}	2.5×10^{34}
	$23.35^{+0.15}_{-0.40}$	$3.40^{+0.40}_{-0.15}$	0.305 ± 0.005	2.7×10^{24}	1.1×10^{44}	2.4×10^{34}

absorption lines to simulate a fake spectrum, fitted it with the continuum model and recorded the best-fitting parameters. This new model for the continuum is then used to simulate the fake data, to reduce uncertainties on the null-hypothesis probability itself (Porquet et al. 2004; Miniutti & Fabian 2006; Markowitz, Reeves & Braito 2006). A new unresolved Gaussian line was included in the model, and its normalization was initially set to zero and free to vary in the range $[-1.0 : +1.0] \times 10^{-4}$ ph cm^{-2} s^{-1}. The energy centroid was free to vary between 7.0 and 10.0 keV in 100 eV steps and the resulting $\Delta\chi^2$ was recorded. If N is the number of data sets in which a chance improvement is found and S is the total number of simulated spectra, then the estimated statistical significance of the detection from Monte Carlo simulations is $1 - N/S$. As an example, we can consider the *NuSTAR* absorption line. Out of the $S =$ 10 000 simulations (both FPMA and B spectra were simultaneously considered), we retrieved $N = 94$ spectra in which a $\Delta\chi^2 \leq -9$ was found. This leads to a statistical significance (1–94/10 000), corresponding to $\simeq 2.6\sigma$ (99.06 per cent confidence level).

When we estimated the statistical significance of the two UFOs (three absorption lines) detected in the 2003 XMM spectrum, we followed the same technique discussed in Longinotti et al. (2015) for IRAS 17020+4544. The detection confidence level for the two lines above 9 keV (UFO 2) is calculated taking into account the absorption line at 8.6 keV (UFO 1), i.e. the input model for the simulations is built adding the UFO 1 component to the continuum. The two statistically significant XMM absorption lines at 8.61 and 9.57 keV are therefore detected with a significance 2.7σ and 3.6σ (99.35 per cent and 99.97 per cent confidence levels), respectively.

3.5 CLOUDY modelling and line identification

NGC 2992 is one of the handful of AGN in which a blueshifted absorption feature is detected with *NuSTAR*. In this section, we discuss the 2015 spectra and the 2003 EPIC pn data, which are both in a medium-high flux state (i.e. 5.8 and 9.5×10^{-11} erg cm^{-2} s^{-1}), using CLOUDY-generated tables. We took into account a self-consistent absorption model to estimate the column density and the ionization state of the UFOs. We produced a grid model for XSPEC using CLOUDY 17, assuming a plane parallel geometry, with the flux of photons striking the illuminated face of the cloud given in terms of ionization parameter U (Osterbrock & Ferland 2006); incident continuum modelled as in Korista et al. (1997); constant electron density $n_e = 10^5$ cm^{-3} and turbulence velocities in the range $v_{turb} = 500-2000$ km s^{-1}. Elemental abundances as in table 7.1 of CLOUDY

documentation[2] and grid parameters are $\log U = [1.00: 5.00]$, $\log N_H = [22.0: 24.0]$.

We start by fitting the high flux 2003 pn spectrum. When the primary continuum is convolved with one CLOUDY component (zone 2), the fit improves ($\Delta\chi^2 = -38/3$ d.o.f.) and the inclusion of a second absorber (zone 1: $\Delta\chi^2 = -18/3$ d.o.f.) leads to a best fit χ^2/d.o.f. $= 147/153 = 0.97$: no strong residuals are seen throughout the 0.5–10 keV band (Fig. 9, bottom panel) and best-fitting values can be found in Table 4. When we leave the turbulence velocity as a variable parameter, no statistical improvement is found and the best-fitting value is $v_{turb} > 650$ km s^{-1}, with the parameter pegging at 2000 km s^{-1}. The outflowing velocity is a free parameter in our CLOUDY components and two distinct velocities are required, $v_1 = 0.215 \pm 0.005c$ and $v_2 = 0.305 \pm 0.005c$.

From a visual inspection of the best-fitting model, the two absorption lines at 9.27 and 9.57 keV can be identified as Fe XXV He α and Fe XXVI Ly α, with outflowing velocities $v_{out} = 0.31 \pm 0.01c$ and $v_{out} = 0.307 \pm 0.006c$, respectively. The third absorption line at 8.61 keV corresponds to Fe XXVI Ly α, with an outflowing velocity $v_{out} = 0.209 \pm 0.006c$ and only an upper limit EW $<$ 40 eV is retrieved for the associated Fe XXV He α component. Fixing the outflow velocity to the one corresponding to Fe XXV He α to the CLOUDY component, a statistically worse fit is obtained ($\Delta\chi^2 = +19/1$ d.o.f.), clearly ruling out this solution. We also show in Table 4 the measured v_{out}/c values, using this identification. We interpret the two absorption lines above 9 keV as Fe XXV He α and Fe XXVI Ly α with same outflowing velocity, but we cannot statistically rule out a fit in which they are modelled in terms of a single broad absorption line, leading to physical scenario with a single outflowing component (still at $v_{out} \sim 0.3c$) with a turbulence velocity $v_{turb} \sim 10\,000$ km s^{-1}.

We then convolved the CLOUDY component (fixing the turbulence velocity to $v_{turb} = 2000$ km s^{-1}) with the model described in Section 3.2, removing the absorption line at 8.26 keV, to reproduce the 2015 *NuSTAR–Swift* data set. We find a very good fit (χ^2/d.o.f. $= 375/415 = 0.91$), with no statistically significant differences with other parameters previously inferred. We find a velocity $v_{out} = 0.21 \pm 0.01c$ for the outflowing gas, a column density $\log (N_H/\text{cm}^{-2}) = 22.25 \pm 0.25$ and a $\log U = 2.45 \pm 0.25$. In this case, the absorption line is identified as Fe XXV He α and the measured $8.26^{+0.09}_{-0.12}$ keV centroid energy (Table 4) can be converted in an outflowing velocity $v_{out} = 0.21 \pm 0.01c$. If we fix the outflow velocity to the

---

[2]Hazy 1 version 17, p. 66: http://viewvc.nublado.org/index.cgi/tags/release/c17.00/docs/hazy1.pdf?revision=11711&root=cloudy
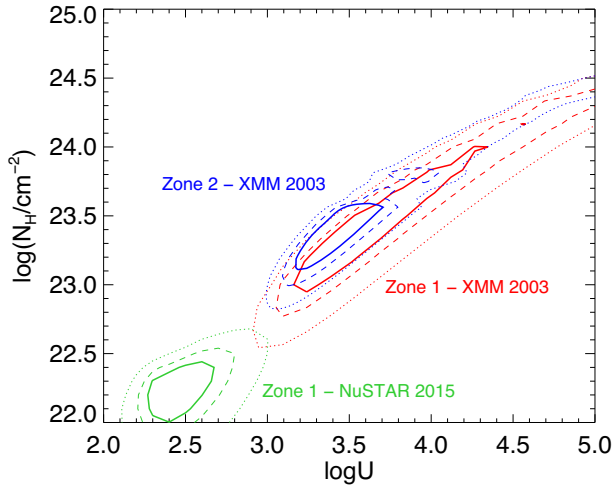
Figure 10. Contour plots between column density and ionization parameter of the two outflowing components for the FPMA/B 2015 (in green) and EPIC pn 2003 spectra (red and blue). Solid, dashed, and dotted lines indicate 68 per cent, 90 per cent, and 99 per cent confidence levels.

Figure 11. Difference spectra of the 2003 and 2010-11-28 observations are shown in black while 2010-05-26 (Obs 3) and 2010-11-28 in red, respectively. Middle and bottom panels contain residuals when an absorbed power-law model is applied to the data sets. Vertical dashed line indicates the rest-frame energy of the neutral Fe K α emission line.

one corresponding to Fe XXVI Ly α to the CLOUDY component, we obtain a worse fit ($\Delta\chi^2 = +13/1$ d.o.f.). The contour plots between the absorbing column density and the ionization parameter can be found in Fig. 10. One absorbing layer (zone 1: $v_{out} \sim 0.21c$) is present in both XMM and *NuSTAR* data sets, while the other (zone 2: $v_{out} \sim 0.30c$) appears only in the very bright state in 2003. The inferred parameters (N_H, U, v_{out}) for the first absorbing zone perfectly fall within the observed range of Ultra Fast Outflows detected with XMM (Tombesi et al. 2010, 2011, 2012) and Suzaku (Gofford et al. 2013, 2015), and are different from the ones found for standard warm absorbers (Tombesi et al. 2013; Laha et al. 2014). The second UFO (zone 2: $v_{out} \sim 0.30c$) is at the upper end of the outflow velocity distribution ($\langle v_{out} \rangle \sim 0.1c$: Tombesi et al. 2010) and it is one of the fastest winds detected in a Seyfert galaxy, at modest accretion rate ($L_{bol}/L_{edd} \simeq 2$–4 per cent). Such velocities are more typically seen around $L_{bol}/L_{edd} \sim 1$ in high luminosity objects (Chartas et al. 2002; Reeves et al. 2009; Tombesi et al. 2015; Reeves et al. 2018) or in NLS1s (Longinotti et al. 2015; Parker et al. 2017a,b, 2018).

4 DISCUSSION

4.1 Origin of the iron K α line

XMM observation no. 7 is one of the historical flux minima of the source and the measured EW of the iron K α line ($EW_7 = 570 \pm 60$ eV) suggests that the primary continuum is very weak, allowing the reflection component to be clearly seen, with a very large reflection fraction ($R = 4.50 \pm 1.10$). We therefore use this spectrum as input background for the 2003 and 2010-05-26 (Obs no. 3) XMM observations to construct difference spectra. Results in the 3–10 keV band are shown in Fig. 11 (top panel, in black and red, respectively), and when fitted with an absorbed power law, the measured values are $N_H^{03} = 0.9 \pm 0.2 \times 10^{22}$ cm^{-2}, $\Gamma^{03} = 1.90 \pm 0.05$ and $N_H^{10} = 1.2 \pm 0.3 \times 10^{22}$ cm^{-2}, $\Gamma^{10} = 1.7 \pm 0.1$. This confirms that the main variable component is the nuclear emission and that it cannot be ascribed to column density changes along the line of sight. The different photon indices indicate that the spectrum is steeper when the source is brighter, as already discussed in Shemmer et al. (2006), Risaliti, Young & Elvis (2009),
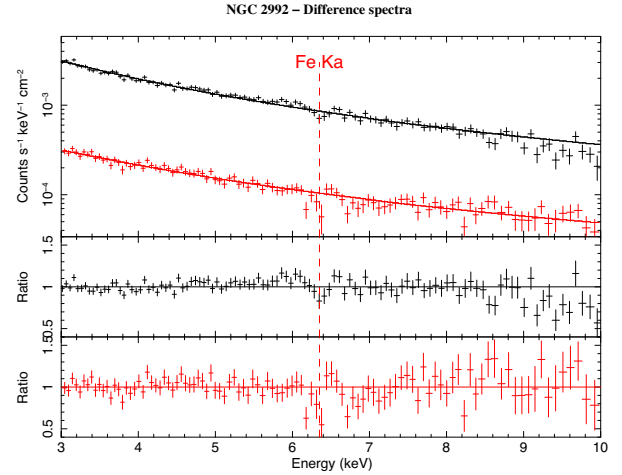
and Ursini et al. (2016). Residuals to this model are shown in middle and bottom panels of Fig. 11, and while strong residuals on the red wing of the Fe K α emission line can be clearly seen in the black data set, they disappear in the 2010 Obs 3, being much more symmetric and centred around ~6.6 keV. Even if we cannot totally discard systematic effects due to the EPIC pn CTI miscalibration, we confirm that no positive residuals on the red wing of the Fe line due to relativistic effects are identified.

Summarizing the spectral analysis reported in Section 3, the iron K α emission line complex in this object is likely the sum of three distinct components:

– a narrow one due to reflection from cold, distant material (likely the molecular torus) which is constant, with a 2–10 keV flux F = $1.25 \pm 0.08 \times 10^{-12}$ erg cm^{-2} s^{-1} and not responding to variations of the primary continuum;

– an unresolved, variable one which is more intense in brighter observations (Obs 3, 9 and NuSTAR 2015). The emitting gas could be located in the outer parts of the accretion disc or in the BLR;

– a relativistic line emitted in the innermost regions of the accretion disc, which has been detected only in the 2003 XMM observation.

The optical emission of this source has been also widely investigated in the past (Veron et al. 1980; Allen et al. 1999; Trippe et al. 2008) and Gilli et al. (2000) interpreted it in terms of a strongly variable underlying continuum with emission lines which are variable in flux but not in width. Indeed, the broad H α FWHM ranges from 2620 km s^{-1} in 1994 (near the X-ray minimum) to 2190 km s^{-1} in 1999 (1.5 months after the BeppoSAX high flux observation). If such material also emitted in the X-rays it would produce an Fe K α emission line with a line width $\sigma \sim 20$ eV, which was not detected in the 2010 low-flux *Chandra* HETG spectra (Murphy et al. 2017). This suggests that the illuminated material (the outskirts of the accretion disc or the BLR) responds to variations of amplitude of the nuclear flux, and the line intensity is hence proportional to the irradiating flux, similarly to what already found for NGC 2110 (Marinucci et al. 2015).

4.2 Energetics of the outflowing winds

The black hole mass of NGC 2992 is estimated to be 5.2×10^7 M$_\odot$ via stellar velocity dispersion measurements (Woo & Urry 2002), which leads to a relative fraction of the Eddington luminosity in the range $L_{bol}/L_{edd} \simeq (0.1–4)$ per cent, using the bolometric correction from Marconi et al. (2004a).

The highest flux states discussed in this paper are the ones observed by *NuSTAR* in 2015 and by *XMM–Newton* in 2003, with 2–10 keV unabsorbed luminosities of 7.6×10^{42}, 1.3×10^{43} erg s^{-1}, with bolometric luminosities $L_{bol} = 1.2 \times 10^{44}$, 2.4×10^{44} erg s^{-1}, corresponding to accretion rates L_{bol}/L_{edd} of 2 per cent and 4 per cent, respectively. The spectral analysis discussed in Section 3.3 showed the presence of strongly blueshifted absorption features only in the 2015 *NuSTAR* and 2003 XMM spectra, i.e. when the accretion rate is larger than $L_{bol}/L_{edd} > 2$ per cent. If modelled with a gas photoionized by the nuclear continuum along the line of sight, we find two accretion disc winds at different velocities ($v_1 \sim 0.2c$ and $v_2 \sim 0.3c$). While the former is in the typical range inferred for UFOs in local Seyfert galaxies (Tombesi et al. 2012; Gofford et al. 2015), the latter is one of the fastest ever detected in a Seyfert galaxy at this low accretion rates.

If we assume that the measured outflowing velocity corresponds to the escape velocity, we can estimate the minimum radius r_{min} at which the accretion disc wind occurs. Following the parametrization on the geometry (conical) and on the density described in Krongold et al. (2007), we can estimate the mass outflow rate $\dot{M}_{out}$ and the kinetic power $\dot{E}_K$ (equations 3 and 4: Tombesi et al. 2013).

For the first wind component (zone 1), found in both the 2015 and 2003 data sets, the outflowing velocity is $v_1 \simeq 65\,000$ km s^{-1} and it corresponds to an emission radius $r_{min} = 3.5 \times 10^{14}$ cm (1.2×10^{-4} pc, or $\sim 25\,r_s$ for a black hole mass $M_{bh} = 5.2 \times 10^7$ M$_\odot$). The lower limits for the mass outflow rate, total kinetic energy rate and momentum rate are reported in Table 4. Assuming the more conservative value for the column density derived for the *NuSTAR* spectra and dividing the inferred $\dot{E}_K$ by the Eddington luminosity ($L_{Edd} = 6.5 \times 10^{45}$ erg s^{-1}), we obtain $\log(\dot{E}_K/L_{Edd}) = -2.9$ which locates this accretion disc wind in the UFO populated region in diagram 2 (left-hand panel) in Tombesi et al. (2013). We find that the total mechanical power $\dot{E}_K \simeq 0.05 L_{bol}$ is sufficient to switch on feedback mechanisms between the AGN and the host galaxy (which can be as low as $\sim 0.005\ L_{bol}$: Di Matteo, Springel & Hernquist 2005; Hopkins & Elvis 2010). We note, however, that if such winds are only triggered at the highest luminosities, their duty cycle is very small, and so will be the feedback effect (Fiore et al. 2017). This value is in perfect agreement with measurements in local sources (Tombesi et al. 2013; Gofford et al. 2015) and much lower than the ones recently found for distant quasars, such as HS 0810+2554 ($z = 1.51$, $\dot{E}_K \approx 9 L_{bol}$: Chartas et al. 2016) and MG J0414+0534 ($z = 2.64$, $\dot{E}_K \approx 2.5 L_{bol}$: Dadina et al. 2018). The total outflow momentum rate can be directly estimated as $\dot{p}_{out} = \dot{M}_{out} v_{out}$ and, if we compare it to the radiation momentum $\dot{p}_{rad} = L_{bol}/c$, we find $\dot{p}_{out} \simeq 0.5\ \dot{p}_{rad}$. This suggest that the wind can be efficiently accelerated in terms of radiation pressure (through Compton scattering; King & Pounds 2003; King 2010b, 2010a).

When we take into account the second wind component (zone 2), only found in the 2003 XMM spectrum, the outflowing velocity is $v_2 \simeq 90\,000$ km s^{-1} and it corresponds to an emission radius $r_{min} = 1.7 \times 10^{14}$ cm (6×10^{-5} pc, or $\sim 10\,r_s$). The total outflow momentum rate from the two wind components is therefore $\dot{p}_{out} \simeq 6\ \dot{p}_{rad}$ possibly indicating an additional/alternative acceler-

ating mechanism, likely due to magnetic torques acting on the wind (Ohsuga et al. 2009; Kazanas et al. 2012; Fukumura et al. 2017).

In NGC 2992, the fast wind features are sporadic, only appearing in the two brightest observations, at accretion rates larger than ~ 2 per cent. The winds are launched in the innermost regions of the accretion disc (assuming that the outflowing velocity corresponds to the escape velocity), at a few tens of gravitational radii. We speculate that the wind can be more effectively accelerated when the luminosity and thus the accretion rate is higher, somehow revealing the innermost regions of the disc. Indeed, such accretion disc winds are accompanied by a broad component of the iron K α emission line. This case is clearly different from other highly accreting objects, such as PDS 456 (Matzeu et al. 2017b, 2017a), where a correlation between the outflowing velocity and the luminosity is observed. Indeed, a response of the relativistic outflowing gas to the variations of the nuclear continuum (in particular the ionization stage) has been recently shown for PDS 456 and IRAS 13224-3809 (Matzeu et al. 2016; Parker et al. 2017a,b, 2018). However, while these two sources are accreting close to L_{Edd}, NGC 2992 is accreting only at a few per cents of the Eddington luminosity.

5 CONCLUSIONS

NGC 2992 has been observed with all major X-ray satellites since 1978 showing a strong variability (up to a factor 20) on timescales of weeks/months. We presented a broadband spectroscopic analysis of eight XMM observations performed in 2010 and one in 2013, of the 2015 simultaneous *Swift* and *NuSTAR* data and of an additional 2003 XMM observation, once corrected for pile-up effects. The source was always in a faint state in 2010/2013 but *NuSTAR* showed an increase in the 2–10 keV flux up to 6×10^{-11} erg cm^{-2} s^{-1} in 2015. Possible evidence of an Ultra Fast Outflow with velocity $v_1 = 0.21 \pm 0.01c$ (at 2.6σ confidence level) is found in this *NuSTAR* observation. This spectral component is not present in the 2010/2013 low-flux spectra, but it is detected in the bright 2003 XMM observation (at 2.7σ confidence level). Using CLOUDY generated tables, the two zones of absorption can be modelled in terms of a highly ionized gas with column densities in the range $N_H = 10^{22}–10^{23}$ cm^{-2} and ionization parameters $\log U = 2.5–3.5$. We find that the total kinetic energy rate of the *NuSTAR* outflow is ≈ 5 per cent L_{bol}, sufficient to switch on feedback mechanisms on the host galaxy. Such accretion disc winds are sporadic in NGC 2992, they arise from a few tens of gravitational radii and have been detected only when the accretion rate of the source exceeds 2 per cent of the Eddington luminosity. This could be indicative of an accretion disc which reveals its innermost regions when the flux rises. In the future, further X-ray observations will test this scenario in more detail.

The analysis of the low flux 2010/2013 XMM data allowed us to determine that the iron K α emission line complex in this object is likely the sum of three distinct components. The first one is narrow and due to reflection from cold, distant material (likely the molecular torus) not responding to variations of the primary continuum and with a constant 2–10 keV flux $F = 1.25 \pm 0.08 \times 10^{-12}$ erg cm^{-2} s^{-1}. The second one is an unresolved, variable component which is more intense in brighter observations (Obs 3 and 9 of the 2010/2013 monitoring campaign). The last one is broad (EW$_{br} = 230^{+60}_{-40}$ eV) and due to relativistic effects in the innermost regions of the accretion disc, only detected in the 2003 XMM observation.

REFERENCES

Allen M. G., Dopita M. A., Tsvetanov Z. I., Sutherland R. S., 1999, ApJ, 511, 686

Arnaud K. A., 1996, George H. Jacoby, and Jeannette Barnes, eds., in ASP Conf. Ser. Vol. 101, Astronomical Data Analysis Software and Systems V. Astron. Soc. Pac., San Francisco, p. 17

Bianchi S., Guainazzi M., Chiaberge M., 2006, A&A, 448, 499

Bianchi S., Chiaberge M., Evans D. A., Guainazzi M., Baldi R. D., Matt G., Piconcelli E., 2010, MNRAS, 405, 553

Cappi M. et al., 2016, A&A, 592, A27

Chartas G., Brandt W. N., Gallagher S. C., Garmire G. P., 2002, ApJ, 579, 169

Chartas G., Cappi M., Hamann F., Eracleous M., Strickland S., Giustini M., Misawa T., 2016, ApJ, 824, 53

Colbert E. J. M., Strickland D. K., Veilleux S., Weaver K. A., 2005, ApJ, 628, 113

Dadina M. et al., 2018, A&A, 610, L13

Dauser T., Garcia J., Wilms J., Böck M., Brenneman L. W., Falanga M., Fukumura K., Reynolds C. S., 2013, MNRAS, 430, 1694

Di Matteo T., Springel V., Hernquist L., 2005, Nature, 433, 604

Fabian A. C., Rees M. J., Stella L., White N. E., 1989, MNRAS, 238, 729

Fabian A. C., Iwasawa K., Reynolds C. S., Young A. J., 2000, PASP, 112, 1145

Ferland G. J. et al., 2017, Rev. Mex. Astron. Astrofis., 53, 385

Fiore F. et al., 2017, A&A, 601, A143

Fukumura K., Kazanas D., Shrader C., Behar E., Tombesi F., Contopoulos I., 2017, Nature Astron., 1, 0062

Gabriel C. et al., 2004, in Ochsenbein F., Allen M. G., Egret D., eds, ASP Conf. Ser. Vol. 314, Astronomical Data Analysis Software and Systems (ADASS) XIII. Astron. Soc. Pac., San Francisco, p. 759

García J., Dauser T., Reynolds C. S., Kallman T. R., McClintock J. E., Wilms J., Eikmann W., 2013, ApJ, 768, 146

Gilli R., Maiolino R., Marconi A., Risaliti G., Dadina M., Weaver K. A., Colbert E. J. M., 2000, A&A, 355, 485

Gofford J., Reeves J. N., Tombesi F., Braito V., Turner T. J., Miller L., Cappi M., 2013, MNRAS, 430, 60

Gofford J., Reeves J. N., McLaughlin D. E., Braito V., Turner T. J., Tombesi F., Cappi M., 2015, MNRAS, 451, 4169

Guainazzi M., Bianchi S., 2007, MNRAS, 374, 1290

Hernández-García L., Masegosa J., González-Martín O., Márquez I., Guainazzi M., Panessa F., 2017, A&A, 602, A65

Hopkins P. F., Elvis M., 2010, MNRAS, 401, 7

Jansen F. et al., 2001, A&A, 365, L1

Kalberla P. M. W., Burton W. B., Hartmann D., Arnal E. M., Bajaja E., Morras R., Pöppel W. G. L., 2005, A&A, 440, 775

Kazanas D., Fukumura K., Behar E., Contopoulos I., Shrader C., 2012, Astron. Rev., 7, 92

Keel W. C., 1996, ApJS, 106, 27

King A. R., 2010a, MNRAS, 408, L95

King A. R., 2010a, MNRAS, 408, L95

King A. R., 2010b, MNRAS, 402, 1516

King A. R., Pounds K. A., 2003, MNRAS, 345, 657

King A., Pounds K., 2015, ARA&A, 53, 115

Korista K., Baldwin J., Ferland G., Verner D., 1997, ApJS, 108, 401

Krongold Y., Nicastro F., Elvis M., Brickhouse N., Binette L., Mathur S., Jiménez-Bailón E., 2007, ApJ, 659, 1022

Laha S., Guainazzi M., Dewangan G. C., Chakravorty S., Kembhavi A. K., 2014, MNRAS, 441, 2613

Longinotti A. L., Krongold Y., Guainazzi M., Giroletti M., Panessa F., Costantini E., Santos-Lleo M., Rodriguez-Pascual P., 2015, ApJ, 813, L39

Marconi A., Risaliti G., Gilli R., Hunt L. K., Maiolino R., Salvati M., 2004a, MNRAS, 351, 169

Marinucci A. et al., 2014b, ApJ, 787, 83

Marinucci A. et al., 2015, MNRAS, 447, 160

Marinucci A. et al., 2016, MNRAS, 456, L94

Marinucci A., Bianchi S., Matt G., Fabian A. C., Iwasawa K., Miniutti G., Piconcelli E., 2011, A&A, 526, A36

Marinucci A., Bianchi S., Fabbiano G., Matt G., Risaliti G., Nardini E., Wang J., 2017, MNRAS, 470, 4039

Markowitz A., Reeves J. N., Braito V., 2006, ApJ, 646, 783

Martocchia A., Matt G., 1996, MNRAS, 282, L53

Matzeu G. A., Reeves J. N., Nardini E., Braito V., Costa M. T., Tombesi F., Gofford J., 2016, MNRAS, 458, 1311

Matzeu G. A., Reeves J. N., Braito V., Nardini E., McLaughlin D. E., Lobban A. P., Tombesi F., Costa M. T., 2017a, MNRAS, 472, L15

Matzeu G. A., Reeves J. N., Nardini E., Braito V., Turner T. J., Costa M. T., 2017b, MNRAS, 465, 2804

Miller J. M. et al., 2010, ApJ, 724, 1441

Miniutti G., Fabian A. C., 2004, MNRAS, 349, 1435

Miniutti G., Fabian A. C., 2006, MNRAS, 366, 115

Moretti A. et al., 2004, in Flanagan K. A., Siegmund O. H. W., eds, Proc. SPIE Conf. Ser. Vol. 5165, X-Ray and Gamma-Ray Instrumentation for Astronomy XIII. SPIE, Bellingham, p. 232

Murphy K. D., Yaqoob T., Terashima Y., 2007, ApJ, 666, 96

Murphy K. D., Nowak M. A., Marshall H. L., 2017, ApJ, 840, 120

Mushotzky R. F., 1982, ApJ, 256, 92

Nardini E., et al., 2015, Science, 347, 860

Nardini E., Porquet D., Reeves J. N., Braito V., Lobban A., Matt G., 2016, ApJ, 832, 45

Negoro H. et al., 2016, Astron. Telegram, 9155

Ohsuga K., Mineshige S., Mori M., Kato Y., 2009, PASJ, 61, L7

Osterbrock D., Ferland G. J., 2006, in Osterbrock D. E., Ferland G. J., eds, Astrophysics of Gaseous Nebulae and Active Galactic Nuclei, University Science Books, Sausalito, CA

Parker M. L., et al., 2014a, MNRAS, 443, 1723

Parker M. L., 2014b, MNRAS, 447, 72

Parker M. L. et al., 2017a, MNRAS, 469, 1553

Parker M. L. et al., 2017b, Nature, 543, 83

Parker M. L., Reeves J. N., Matzeu G. A., Buisson D. J. K., Fabian A. C., 2018, MNRAS, 474, 108

Piconcelli E., Jimenez-Bailón E., Guainazzi M., Schartel N., Rodríguez-Pascual P. M., Santos-Lleó M., 2004, MNRAS, 351, 161

Porquet D., Reeves J. N., Uttley P., Turner T. J., 2004, A&A, 427, 101

Protassov R., van Dyk D. A., Connors A., Kashyap V. L., Siemiginowska A., 2002, ApJ, 571, 545

Reeves J. N. et al., 2009, ApJ, 701, 493

Reeves J. N., Braito V., Nardini E., Lobban A. P., Matzeu G. A., Costa M. T., 2018, ApJ, 854, L8

Reynolds C. S., 2014, Space Sci. Rev., 183, 277

Reynolds C. S., Nowak M. A., 2003, Phys. Rep., 377, 389

Risaliti G., Elvis M., Fabbiano G., Baldi A., Zezas A., 2005, ApJ, 623, L93

Risaliti G., Young M., Elvis M., 2009, ApJ, 700, L6

Shemmer O., Brandt W. N., Netzer H., Maiolino R., Kaspi S., 2006, ApJ, 646, L29

Shu X. W., Yaqoob T., Murphy K. D., Braito V., Wang J. X., Zheng W., 2010, ApJ, 713, 1256

Strüder L. et al., 2001, A&A, 365, L18

Tombesi F., Cappi M., Reeves J. N., Palumbo G. G. C., Yaqoob T., Braito V., Dadina M., 2010, A&A, 521, A57

Tombesi F., Cappi M., Reeves J. N., Palumbo G. G. C., Braito V., Dadina M., 2011, ApJ, 742, 44

Tombesi F., Cappi M., Reeves J. N., Braito V., 2012, MNRAS, 422, L1

Tombesi F., Cappi M., Reeves J. N., Nemmen R. S., Braito V., Gaspari M., Reynolds C. S., 2013, MNRAS, 430, 1102

Tombesi F., Meléndez M., Veilleux S., Reeves J. N., González-Alfonso E., Reynolds C. S., 2015, Nature, 519, 436

Trippe M. L., Crenshaw D. M., Deo R., Dietrich M., 2008, AJ, 135, 2048

Turner M. J. L. et al., 2001, A&A, 365, L27

Ursini F. et al., 2016, MNRAS, 463, 382

Vaughan S. et al., 2006, ApJ, 638, 920

Veron P., Lindblad P. O., Zuiderwijk E. J., Veron M. P., Adam G., 1980, A&A, 87, 245

Walton D. J. et al. 2014, ApJ, 788, 76

Walton D. J. et al., 2016, ApJ, 826, L26

Weaver K. A., Nousek J., Yaqoob T., Mushotzky R. F., Makino F., Otani C., 1996, ApJ, 458, 160

Wilkins D. R., Fabian A. C., 2012, MNRAS, 424, 1284

Woo J., Urry C. M., 2002, ApJ, 579, 530

Yaqoob T., Murphy K. D., Terashima Y., 2007, in Karas V., Matt G., eds, Proc. IAU Symp., 238, Black Holes from Stars to Galaxies – Across the Range of Masses, Cambridge University Press, Cambridge, UK. p. 123

APPENDIX

In this appendix, we discuss instrumental effects induced by pile-up in the 2003 XMM observation. NGC 2992 was targeted by XMM in full-frame mode in 2003, for a total elapsed time of 27 ks. With an average 0.5–10 keV count rate of 19.32 ± 0.39 cts s^{-1}, the observation was inevitably affected by pile-up. We reduced the data set following the same approach described in Section 2.1 (for calculating source extraction radius, optimal time cuts for flaring particle background and energy binning) without pile-up corrections. This spectrum (not excised) was then compared to the one used for our analysis, in which pile-up is removed. In principle, there is no reason to expect that pile-up could create narrow line-like spurious features, it produces a flatter spectral shape, due to the false detection of soft X-ray photons at higher energies. We therefore fitted the two spectra with a phenomenological model composed of a power law plus a narrow Gaussian line at 6.4 keV, in the 3–10 keV band. As expected, we obtain a harder photon index for the piled-up spectrum ($\Gamma_1 = 1.50 \pm 0.01$), compared to the one in which such an instrumental effect is removed ($\Gamma_2 = 1.72 \pm 0.02$). The high-energy UFO features in NGC 2992 are completely smeared out in the piled-up spectrum and also part of the broad component of the Fe K α is hidden, as already discussed in Miller et al. (2010). They appear in the pile-up corrected spectrum and, even if we exclude the central region of the source up to 15 arcsec (instead of 10 arcsec, as in Shu et al. 2010), we find the same slope for the continuum compared to the one reported in Section 3.3 and the same absorption features, with larger uncertainties.

This paper has been typeset from a TeX/LaTeX file prepared by the author.